Structure-property relationship of reversible magnetic chirality tuning

Jing Qi [1], Paula M. Weber [1], Tilman Kißlinger,[2] Lutz Hammer [2], M. Alexander Schneider [2,*] and Matthias Bode [1,3,†]

[1]*Physikalisches Institut, Experimentelle Physik II, Julius-Maximilians-Universität Würzburg, Am Hubland, 97074 Würzburg, Germany*
[2]*Solid State Physics, Friedrich-Alexander-Universität Erlangen-Nürnberg, Staudtstrasse 7, 91058 Erlangen, Germany*
[3]*Wilhelm Conrad Röntgen-Center for Complex Material Systems (RCCM),
Julius-Maximilians-Universität Würzburg, Am Hubland, 97074 Würzburg, Germany*

The Ruderman-Kittel-Kasuya-Yosida (RKKY) interaction mediates collinear magnetic interactions via the conduction electrons of a nonmagnetic spacer, resulting in a ferro- or antiferromagnetic magnetization in magnetic multilayers. Recently it has been discovered that heavy nonmagnetic spacers are able to mediate an indirect magnetic coupling that is noncollinear and chiral. This Dzyaloshinskii-Moriya-enhanced RKKY interaction causes the emergence of a variety of interesting magnetic structures, such as skyrmions and spin spirals. Here, we show by spin-polarized scanning tunneling microscopy that the interchain coupling between manganese oxide chains on Ir(001) can reproducibly be switched from chiral to collinear antiferromagnetic by increasing the oxidation state of MnO_2, while the reverse process can be induced by thermal reduction. The underlying structure–property relationship is revealed by low-energy electron diffraction intensity analysis. Density functional theory calculations suggest that the magnetic transition may be caused by a significant increase of the Heisenberg exchange which overrides the Dzyaloshinskii-Moriya interaction upon oxidation.

Introduction. Driven by the discovery of spin-polarized charge transport, such as the giant magnetoresistance effect, the coupling between magnetic layers separated by nonmagnetic spacers attracted considerable interest over the past 40 years [1,2]. It was soon realized that the interlayer exchange coupling is governed by the Ruderman-Kittel-Kasuya-Yosida (RKKY) coupling [3–6]. Whereas the conventional RKKY interaction exclusively results in collinear magnetism, i.e., ferromagnetic (FM) or antiferromagnetic (AFM) coupling [7], another long predicted [8], yet only recently discovered interaction is able to mediate a chiral magnetic coupling between magnetic chains [9,10] or layers [11–13], respectively. Similar to conventional collinear RKKY, this novel interaction is also mediated by conduction electrons of a nonmagnetic spacer which are polarized by the magnetic material. Due to the high spin-orbit coupling of the spacer, however, a Dzyaloshinskii-Moriya (DM) type enhancement takes place [8], resulting in an asymmetric indirect exchange interaction.

This *DM-enhanced RKKY* (DME-RKKY) interaction, also called *interlayer DMI* in layered systems [12,13], is fundamentally different from the more common *interfacial DMI* which results from the combination of strong spin-orbit coupling and broken inversion symmetry [14,15]. The DME-RKKY interaction is of high fundamental and practical interest. For example, it may "provide the capability to further tailor topological spin textures, in not only one-dimensional (1D) or two-dimensional (2D) but also 3D space" [16], such as skyrmions which are robust against thermal or quantum fluctuations [17]. This may potentially enable novel spintronic

applications, such as racetrack memories [18], spin valves with heavy-metal cap layers [19], or spin-orbit torque-based logic devices [20].

Whether or not chiral spin structures form, however, critically depends on the balance between the DMI and other interactions, such as the exchange interaction and the magnetocrystalline anisotropy. Particularly fascinating and promising for applications are concepts where this balance can reversibly be fine-tuned by an external stimulus. Various methods have been proposed, including tuning of the oxygen coverage [21], hydrogen adsorption [22], or the application of electric fields [23]. Although experimental implementations have been reported for systems with interfacial DMI [24,25], these concepts have not yet been realized in the context of the DME-RKKY interaction.

MnO_x on Ir(001) is the ideal testbed towards a better understanding of the structure–property relationship which drives the transition between chiral and collinear spin structures, as the surface character of all constituents allows for the direct probing of structural and magnetic properties which are difficult to obtain in buried multilayer films [24,25]. Here we reveal by spin-polarized scanning tunneling microscopy (SP-STM) that the MnO_x interchain coupling can reversely be switched between chiral and collinear AFM by tuning the oxygen partial pressure p_{O_2} during preparation. This transition can directly be linked to specific structural properties by an analysis of the energy-dependent intensity of low-energy electron diffraction beams (LEED-IV). Our study reveals that the different spin configurations arise from a structural transition from MnO_2 at low p_{O_2} to MnO_3 chains with the addition of another oxygen atom at the Ir bridge site, O_{br}, at high p_{O_2}. Our work presents a new path toward "spin orbitronics" [22] by introducing a reversible and reproducible manipulation of the

*Corresponding author: alexander.schneider@fau.de
†Corresponding author: bode@physik.uni-wuerzburg.de
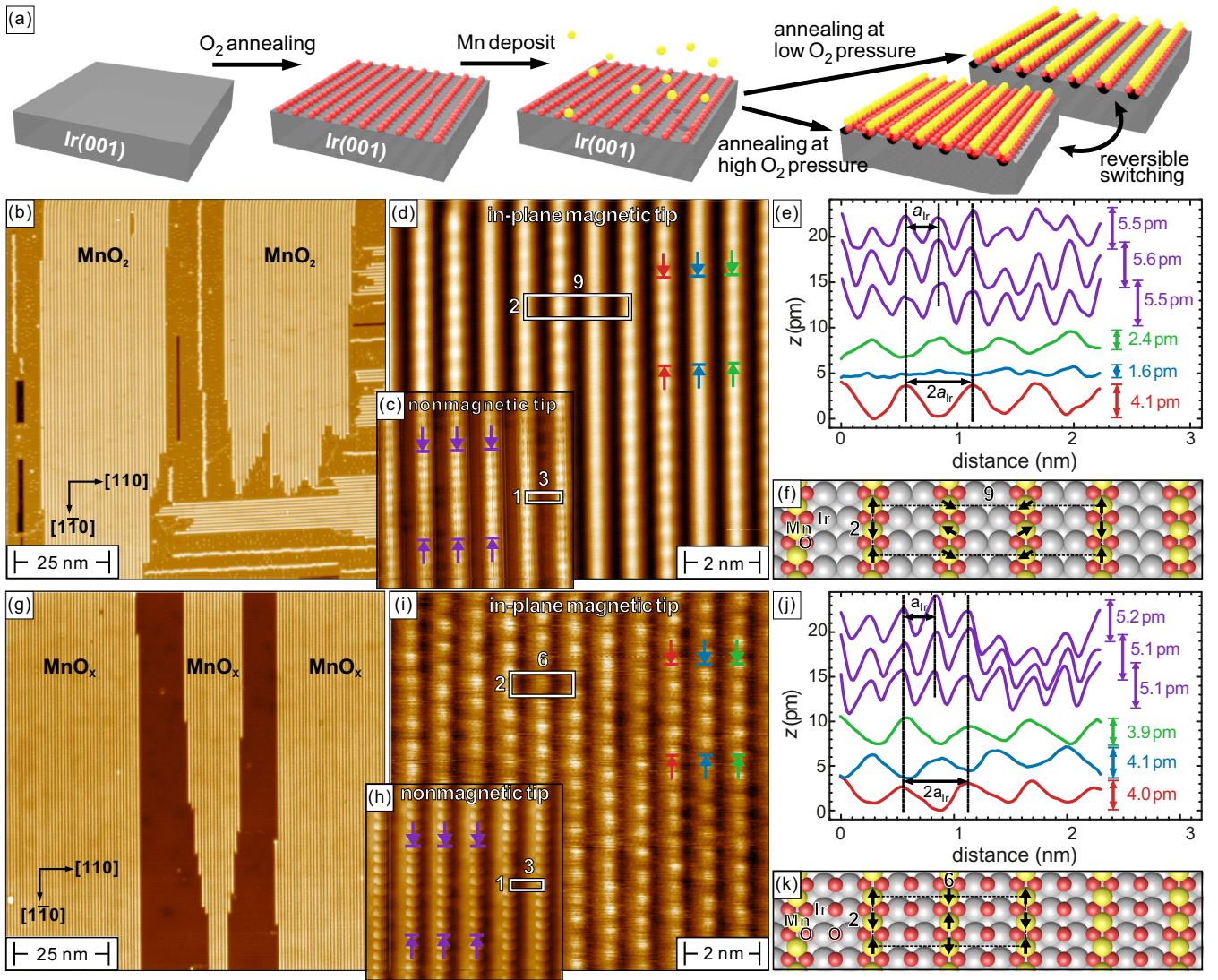
FIG. 1. (a) Scheme of the sample preparation procedures. Depending on the oxygen pressure p_{O_2} during the final annealing step, different MnO$_x$ stoichiometries with $x = 2$ or $x > 2$ are obtained. (b) Large-scale STM topographic image of a sample prepared at low p_{O_2}. MnO$_2$ chains are oriented along the [110] and [1$\bar{1}$0] direction of Ir(001) (scan parameters: $U = 100$ mV, $I = 500$ pA). (c),(d) Atomic resolution images scanned with a nonmagnetic tungsten tip and a magnetic Mn tip ($U = 100$ mV, $I = 1$ nA). (e) Line profiles measured on the chains indicated by colored markers in (c) and (d) showing a doubling of the a_{Ir} period in (d) as well as a systematic variation of amplitudes and phases between green, blue, and red line profiles, characteristic for chiral magnetic order across MnO$_2$ chains. (f) Model of the (9×2) MnO$_2$ structure. Gray, red, and yellow spheres represent Ir, O, and Mn atoms, respectively. Mn spin orientation is marked by black arrows. (g) Large scale STM image of a similar surface as in (a), but prepared at high p_{O_2} ($U = 100$ mV, $I = 50$ pA). (h),(i) Atomic resolution STM images of the $c(6 \times 2)$ MnO$_x$ chain structure scanned with a nonmagnetic and a Mn-coated magnetic tip, respectively [(h) $U = 50$ mV, $I = 1$ nA; (i) $U = 300$ mV, $I = 0.5$ nA]. (j) Line profiles along the lines in (h) and (i), showing a doubling of the periodicity in (i) compared to that of (h) and an antiphase relation between neighboring rows. (k) Model of the $c(6 \times 2)$ MnO$_x$ structure.

magnetic structure in indirectly coupled magnetic transition-metal oxides via chemically tuning their stoichiometry.

Sample preparation. The four-steps sample preparation procedure is schematically represented in Fig. 1(a). It consists of (i) the preparation of clean Ir(001), (ii) the formation of an oxygen-terminated Ir(001)–(2 × 1) adsorbate structure, (iii) submonolayer (ML) Mn deposition, and (iv) a final oxygen annealing step. We found that the oxygen pressure during this concluding step is decisive for the stoichiometry of the resulting MnO$_x$ chains. Whereas a high exposure of ≈13.5 Langmuir (L) at $p_{O_2} \geqslant 1 \times 10^{-7}$ mbar yields an

oxygen-rich MnO$_{x>2}$ structure, exposure to ≈1.3 L at $p_{O_2} \leqslant 5 \times 10^{-8}$ mbar gives the oxygen-poor MnO$_2$ structure. A careful discussion of the transferability of the preparation parameters between the different laboratories, SP-STM and LEED-IV data acquisition and analysis, as well as density functional theory (DFT) procedures is provided in Ref. [26].

Experimental results (STM). Figures 1(b)–1(d) present spin-averaged and SP-STM results obtained on MnO$_2$ chains prepared at low p_{O_2}. Figure 1(b) shows a typical overview STM topographic image of a sample partially covered by

MnO_2 chains. The chains are highly ordered, periodic, and oriented along the Ir [110] and [1$\bar{1}$0] directions. Previous studies showed that the Mn atoms reside above a missing-row structure and only indirectly interact with the Ir substrate via oxygen atoms. Each Mn atom is coordinated to four surrounding oxygen atoms, which in turn bind to one substrate Ir atom and two Mn atoms [27]. Figure 1(c) shows an atomically resolved STM image of the MnO_2 chains scanned with a nonmagnetic tungsten tip. We recognize a (3×1) unit cell (white rectangle), in agreement with published data [9,10,27]. Line profiles along three adjacent MnO_2 chains marked by purple markers in Fig. 1(c) are presented in the upper part of Fig. 1(e). The periodicity is consistent with the Ir lattice constant $a_{Ir} \approx 2.71$ Å.

Figure 1(d) shows a corresponding data set, but scanned with a spin-sensitive tip. In good agreement with Ref. [9] we recognize a magnetic (9×2) unit cell (white rectangle). Line profiles taken along three adjacent MnO_2 chains reveal that the periodicity has doubled to $2a_{Ir}$; see lower part of Fig. 1(e). The corrugation amplitude along the chains systematically varies between 1.6 pm and 4.1 pm and the line profiles are phase shifted to one another. As sketched in Fig. 1(f), these observations can consistently be explained [9] by a magnetic (9×2) unit cell caused by collinear AFM order along the chains and a chiral 120° spin spiral perpendicular to the chains.

Figure 1(g) shows a typical large-scale STM image of a sample prepared similar to the one presented in Fig. 1(b), but with a final annealing step performed at high p_{O_2}. We again find chains which are highly ordered, periodic, and oriented along the Ir [110] and [1$\bar{1}$0] directions. Since the final annealing step ($T_{ann} = 1020$ K) was performed at high p_{O_2}, and since the MnO_2 chains only decompose in vacuum at $T > 1070$ K, we speculate that the oxygen excess results in the formation of $MnO_{x>2}$. This assumption will be confirmed below by LEED-IV structural analysis. Figure 1(h) shows atomically resolved data of $MnO_{x>2}$ chains scanned with a nonmagnetic tip. We recognize a (3×1) unit cell (white rectangle), i.e., the same as in Fig. 1(c). Line profiles along three adjacent $MnO_{x>2}$ chains indicated by purple markers in Fig. 1(h) are shown in the upper part of Fig. 1(j). Again, the periodicity agrees with a_{Ir}. The striking resemblance of Fig. 1(h) and Fig. 1(c) implies that the Mn core of the oxide chain remains unchanged.

Yet SP-STM data of the $MnO_{x>2}$ chain structure now reveal a $c(6 \times 2)$ unit cell (white rectangle); see Fig. 1(i). Line profiles along three adjacent $MnO_{x>2}$ chains marked in Fig. 1(i) are shown in the lower part of Fig. 1(j). A $2a_{Ir}$ periodicity and a π phase shift between adjacent chains are immediately apparent. To reveal the structural differences even clearer, we compared the two structures by calculating the respective 2D Fourier transformed STM topographic images, showing different periodicities in the reciprocal features (see Ref. [26] for exemplary results). Furthermore, unlike for MnO_2 in Fig. 1(d), the corrugation of (4.0 ± 0.1) pm remains the same for all $MnO_{x>2}$ chains. These observations imply a spin structure which is not only collinear AFM along the chains, but also collinear across adjacent chains. Figure 1(k) shows this presumed spin structure of $MnO_{x>2}$ with its $c(6 \times 2)$ magnetic unit cell [28].
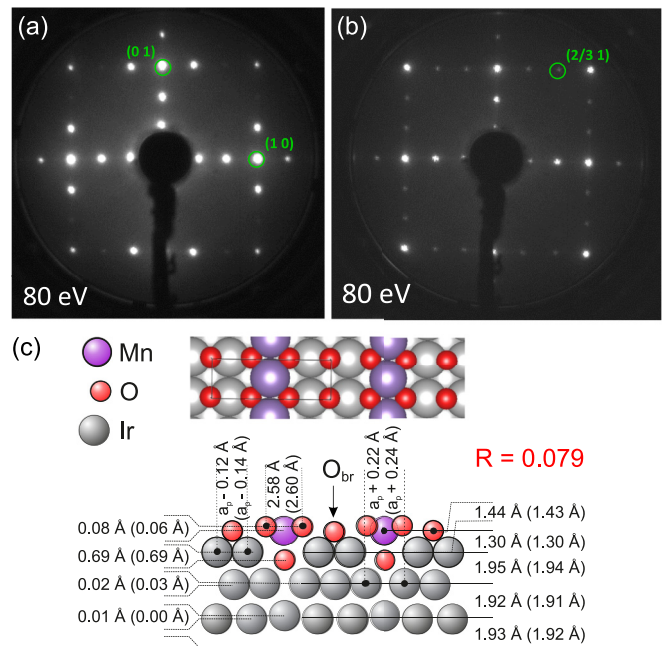
FIG. 2. LEED patterns of 1/3 ML Mn oxidized in (a) $p_{O_2} = 5 \times 10^{-8}$ mbar molecular O_2 and (b) in $p_{NO_2} = 1 \times 10^{-6}$ mbar (for exact conditions see text). The intensity spectrum of the spot marked in (b) is shown in Fig. 3. (c) Top and side view of the (3×1) $MnO_3 + O_{br}$ structure and relevant structural parameters as obtained by LEED-IV structural analysis of the preparation in (b). The resulting parameters of the DFT energy minimization are given in brackets.

Importantly, we were able to reversibly and repeatedly switch between the collinear AFM spin structure of $c(6 \times 2)$ $MnO_{x>2}$ and the noncollinear, chiral (9×2) MnO_2 chains by annealing at $T_{ann} = 1020$ K in high or low p_{O_2}, respectively (see Ref. [26] for exemplary results). We would like to highlight that this transition does not require any further Mn supply, indicating that only the oxidation state changes whereas the Mn remains on the Ir(001) surface, without any desorption into the gas phase or diffusion into the substrate.

Experimental results (LEED-IV). It is evident that the two distinct magnetic unit cells observed for MnO_x chains prepared by high and low p_{O_2} must have a structural reason. Based on our previous work on the CoO_x chains on Ir(001) [29], we expected that MnO_2 could also be further oxidized to MnO_3. However, for Co this was only achieved with an oxidizing agent (NO_2) that provides O atoms easily [29]. We therefore first checked if MnO_3 chains could be produced from MnO_2 by oxidation with NO_2. To obtain the crystallographic structure from LEED-IV analysis with high quality and low error margins, we deposited 1/3 ML Mn/Ir(001), which leads to a surface homogeneously covered with MnO_2 chains in a (3×1) superstructure after oxidation in $p_{O_2} = 5 \times 10^{-8}$ mbar. A LEED pattern of this surface is presented in Fig. 2(a). Comparison to LEED spectra obtained previously [27] confirms that the chains have the expected MnO_2 structure. Subsequently, we oxidized the surface in $p_{NO_2} = 10^{-6}$ mbar at 870 K and performed two annealing steps at 530 K. The final cooldown was carried out without NO_2 flux to ensure the desorption of remaining NO_x from the
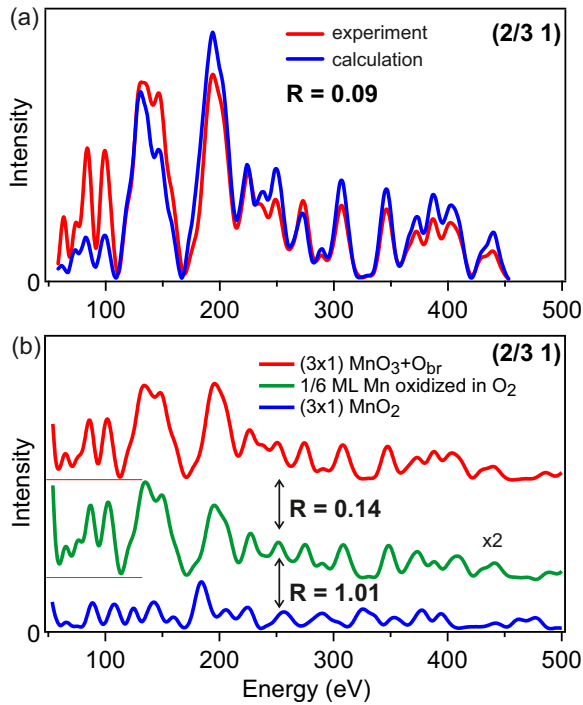
FIG. 3. Intensity spectra of the $k_{||} = (2/3\ 1)$ beam. (a) Comparison of the normalized intensity between the experimental (red) and the calculated (blue) spectrum of the MnO_3+O_{br} structure (single beam R factor $R = 0.091$). (b) Comparison between experimental spectra obtained from the $(3 \times 1)MnO_2$ at 13 ML Mn (lowest curve, blue) of the $(3 \times 1)MnO_3+O_{br}$ prepared by oxidation in NO_2 (top curve, red), and a preparation comparable to that when the $c(6 \times 2)$ magnetic supercell occurs (middle curve, green). The middle curve is scaled by a factor of 2. The visual agreement between the middle and upper curve is substantiated by an R factor of $R = 0.14$. Curves in (b) are offset for clarity.

surface. The LEED image of the resulting surface is shown in Fig. 2(b). Again, a (3×1) LEED pattern is observed with, however, very different spot intensities. This unambiguously proves a changed surface structure. A LEED-IV analysis with a Pendry R factor of $R = 0.083$ reveals that the structure obtained after NO_2 oxidation is indeed the expected MnO_3 chain structure (analogous to CoO_3 [29]), only with the important difference that the Ir bridge sites between the chains are all occupied by additional oxygen atoms (with error margin of 17%). The model was also tested in a structural relaxation calculation using DFT. All structural parameters determined experimentally agree within the single-digit picometer range to the calculated values after scaling the DFT a_{Ir} lattice parameter to the experimental one [Fig. 2(c)]. An example of the excellent agreement between measured and calculated LEED spectra is shown in Fig. 3(a). For the complete data set, see Ref. [26].

For an Ir(001) surface fully covered with MnO_2 chains, further oxidation in O_2 was impossible up to $p_{O_2} = 10^{-6}$ mbar, i.e., the chains remained in their MnO_2 state. Only for partially covered surfaces, e.g., at 1/6 ML Mn, did further oxidation become possible. We suspect that partially covered Ir(001) provides (defect) sites for O_2 dissociation. However,

the reduced order also complicates the LEED-IV analysis. The proof of oxidation becomes possible when looking at the third-order diffraction spots that do not contain intensity contributions from the coexisting $(2 \times 1)O$ phase. This is shown in Fig. 3(b) for the $k_{||} = (2/3, 1)$ spots. Visual inspection of the spectra already reveals that those of the highly oxidized phase at 1/6 ML Mn belong to the pure (1/3 ML) MnO_3+O_{br} rather than to the MnO_2 phase. An R factor analysis between a set of experimental third-order beams of the 1/6 ML phase and the MnO_3+O_{br} structure yields $R = 0.14$, whereas the MnO_2 structure gives $R = 0.81$ [26]. We can therefore be confident that the preparation with 1/6 ML Mn oxidized at $p_{O_2} = 10^{-6}$ mbar results in the MnO_3+O_{br} phase and that this structure gives rise to the $c(6 \times 2)$ magnetic unit cell observed in Figs. 1(g)–1(i). Furthermore, a phase stability analysis by DFT [29–31] supports the view that only the MnO_3+O_{br} and MnO_2 chains appear as stable phases [26].

Discussion. The SP-STM results presented in Fig. 1 show that the magnetic order across adjacent MnO_x chains can controllably and reversibly be switched between a collinear AFM and a noncollinear chiral state by annealing at high or low p_{O_2}, respectively. Structural LEED-IV analysis reveals that this different interchain coupling comes along with a different surface stoichiometry. While samples annealed at low p_{O_2} exhibit MnO_2 chains, annealing at high p_{O_2} results in a higher oxidation state, where a third O atom is relaxed in the vacancy row underneath the Mn atom and another O occupies the Ir bridge site midway between the MnO_3 chains.

The chiral $120°$ magnetic coupling observed between MnO_2 chains across the intermediate Ir(001) substrate was explained by the DME-RKKY interaction [9]. We have to bear in mind, however, that a chiral spin structure can only develop if the DMI is able to overcome the Heisenberg exchange interaction J and the anisotropy K [32,33]. In a slightly simplified picture the transition occurs at $D^2 > 4JK$ [32]. Since J is extremely small for MnO_2/Ir(001) (≈ 1 meV per Mn atom), the DMI can trigger the spin spiral state observed in Fig. 1(d) [9,27].

To get an idea of the relevant J values which drive the transition to the collinear state for TMO chains with the stoichiometry $MnO_{x>2}$, we calculated the magnetic intra- and interchain coupling for MnO_2, MnO_3, a hypothetical MnO_2+O_{br}, and the MnO_3+O_{br} structures using spin-resolved, collinear DFT$+U$. All structures show a strong AFM intrachain coupling of 20 to 30 meV per Mn atom, in agreement with our experimental findings presented in Figs. 1(d) and 1(i). The interchain coupling quantitatively depends on the amount of oxygen in the surface structure. As reported before, we calculate a weak AFM interchain coupling of ≈ 1.5 meV per atom for the MnO_2 chains [27]. This coupling essentially vanishes for the hypothetical MnO_2+O_{br} structure. For the MnO_3 structure we find a much stronger AFM interchain coupling of 7 meV per atom, and eventually a FM interchain coupling of 5 meV when the O_{br} is added. Despite the fact that a (3×2) magnetic cell is predicted by DFT for the experimentally found MnO_3+O_{br}, the results clearly show that indirect coupling via the substrate is substantially increased by the additional oxygen atom underneath the Mn atom. The O_{br} adds a second interference path for the RKKY interaction and may change size and sign of the

interchain interaction. To resolve the discrepancy with respect to the experimentally observed magnetic cells, we suggest to use our robust structural analysis as a basis for more refined calculations which also consider noncollinear magnetic order and spin-orbit coupling.

In summary, we presented a combined SP-STM and IV-LEED study which resolves the structure-property relationship of MnO_x chains on Ir(001), a surface-accessible sample system which for $x = 2$ exhibits a chiral interchain coupling driven by the DME-RKKY interaction. We find that oxidation at high p_{O_2} results in MnO_3 chains with additional O_{br} on the Ir(001) substrate between the chains. DFT calcula-

tions confirm that the higher oxygen content results in a strong enhancement of the Heisenberg exchange interaction, probably sufficient to override the weak DME-RKKY interaction responsible for chiral magnetic order at low oxygen content. Our study provides an addition to the toolbox of tailoring topological spin textures by the DME-RKKY interaction.

[1] A. Fert, P. Grünberg, A. Barthélémy, F. Petroff, and W. Zinn, Layered magnetic structures: Interlayer exchange coupling and giant magnetoresistance, J. Magn. Magn. Mater. **140-144**, 1 (1995).

[2] M. D. Stiles, Interlayer exchange coupling, J. Magn. Magn. Mater. **200**, 322 (1999).

[3] M. A. Ruderman and C. Kittel, Indirect exchange coupling of nuclear magnetic moments by conduction electrons, Phys. Rev. **96**, 99 (1954).

[4] T. Kasuya, A theory of metallic ferro- and antiferromagnetism on Zener's model, Prog. Theor. Phys. **16**, 45 (1956).

[5] K. Yosida, Magnetic properties of Cu-Mn alloys, Phys. Rev. **106**, 893 (1957).

[6] T. Moriya, Anisotropic superexchange interaction and weak ferromagnetism, Phys. Rev. **120**, 91 (1960).

[7] P. Bruno and C. Chappert, Oscillatory Coupling between Ferromagnetic Layers Separated by a Nonmagnetic Metal Spacer, Phys. Rev. Lett. **67**, 1602 (1991).

[8] A. Fert and P. M. Levy, Role of Anisotropic Exchange Interactions in Determining the Properties of Spin-Glasses, Phys. Rev. Lett. **44**, 1538 (1980).

[9] M. Schmitt, P. Moras, G. Bihlmayer, R. Cotsakis, M. Vogt, J. Kemmer, A. Belabbes, P. M. Sheverdyaeva, A. K. Kundu, C. Carbone, S. Blügel, and M. Bode, Indirect chiral magnetic exchange through Dzyaloshinskii-Moriya-enhanced RKKY interactions in manganese oxide chains on Ir(100), Nat. Commun. **10**, 2610 (2019).

[10] M. Schmitt, C. H. Park, P Weber, A. Jäger, J. Kemmer, M. Vogt, and M. Bode, Structural and magnetic properties of 3*d* transition metal oxide chains on the (001) surfaces of Ir and Pt, Phys. Rev. B **100**, 054431 (2019).

[11] S. V. Grigoriev, Yu. O. Chetverikov, D. Lott, and A. Schreyer, Field Induced Chirality in the Helix Structure of Dy/Y Multilayer Films and Experimental Evidence for Dzyaloshinskii-Moriya Interaction on the Interfaces, Phys. Rev. Lett. **100**, 197203 (2008).

[12] D.-S. Han, K. Lee, J.-P. Hanke, Y. Mokrousov, K.-W. Kim, W. Yoo, Y. L. W. van Hees, T.-W. Kim, R. Lavrijsen, C.-Y. You, H. J. M. Swagten, M.-H. Jung, and M. Kläui, Long-range chiral exchange interaction in synthetic antiferromagnets, Nat. Mater. **18**, 703 (2019).

[13] A. Fernández-Pacheco, E. Vedmedenko, F. Ummelen, R. Mansell, D. Petit, and R. P. Cowburn, Symmetry-breaking interlayer Dzyaloshinskii–Moriya interactions in synthetic antiferromagnets, Nat. Mater. **18**, 679 (2019).

[14] A. Fert, N. Reyren, and V. Cros, Magnetic skyrmions: advances in physics and potential applications, Nat. Rev. Mater. **2**, 17031 (2017).

[15] H. Yang, A. Thiaville, S. Rohart, A. Fert, and M. Chshiev, Anatomy of Dzyaloshinskii-Moriya Interaction at Co/Pt Interfaces, Phys. Rev. Lett. **115**, 267210 (2015).

[16] T. Dohi, R. M. Reeve, and M. Kläui, Thin film skyrmionics, Annu. Rev. Condens. Matter Phys. **13**, 73 (2022).

[17] H.-B. Braun, Topological effects in nanomagnetism: from superparamagnetism to chiral quantum solitons, Adv. Phys. **61**, 1 (2012).

[18] F. Ummelen, H. Swagten, and B. Koopmans, Racetrack memory based on in-plane-field controlled domain-wall pinning, Sci. Rep. **7**, 833 (2017).

[19] J. Du, M. Li, and J. Lu, Stabilizing current-driven steady flows of 180° domain walls in spin valves by interfacial Dzyaloshinskii-Moriya interaction, Phys. Rev. B **103**, 144429 (2021).

[20] Y. Shi, K. Chi, Z. Li, W. Zhang, Y. Xing, H. Meng, and B. Liu, Reconfigurable spin orbit logic device using asymmetric Dzyaloshinskii–Moriya interaction, Appl. Phys. Lett. **117**, 072401 (2020).

[21] A. Belabbes, G. Bihlmayer, S. Blügel, and A. Manchon, Oxygen-enabled control of Dzyaloshinskii-Moriya interaction in ultra-thin magnetic films, Sci. Rep. **6**, 24634 (2016).

[22] B. Yang, Q. Cui, J. Liang, M. Chshiev, and H. Yang, Reversible control of Dzyaloshinskii-Moriya interaction at the graphene/Co interface via hydrogen absorption, Phys. Rev. B **101**, 014406 (2020).

[23] H. Yang, O. Boulle, V. Cros, A. Fert, and M. Chshiev, Controlling Dzyaloshinskii-Moriya interaction via chirality dependent atomic-layer stacking, insulator capping and electric field, Sci. Rep. **8**, 12356 (2018).

[24] G. Chen, M. C. Robertson, M. Hoffmann, C. Ophus, A. L. Fernandes Cauduro, R. Lo Conte, H. Ding, R. Wiesendanger, S. Blügel, A. K. Schmid, and K. Liu, Observation of Hydrogen-Induced Dzyaloshinskii-Moriya Interaction and Reversible Switching of Magnetic Chirality, Phys. Rev. X **11**, 021015 (2021).

[25] G. Chen, C. Ophus, A. Quintana, H. Kwon, C. Won, H. Ding, Y. Wu, A. K. Schmid, and K. Liu, Reversible writing/deleting of magnetic skyrmions through hydrogen adsorption/desorption, Nat. Commun. **13**, 1350 (2022).

[26] See Supplemental Material at http://link.aps.org/supplemental/10.1103/PhysRevB.107.L060409 for detailed information re-

garding the sample preparation procedures, experimental and computational setups, comparison between the two structures of their STM topographic images and 2D Fourier transformed images, STM data of reversible switch between (9×2) MnO_2 and $c(6 \times 2)MnO_{x>2}$ magnetic spin structures, results of the structural LEED-IV analysis for the well-prepared Ir(100)-3 $\times$ 1-MnO_3 + O_{br} phase, an *R*-factor comparison of IV spectra taken for differently prepared samples, and a phase stability analysis by DFT, which includes Refs. [34–49].

[27] P. Ferstl, L. Hammer, C. Sobel, M. Gubo, K. Heinz, M. A. Schneider, F. Mittendorfer, and J. Redinger, Self-Organized Growth, Structure, and Magnetism of Monatomic Transition-Metal Oxide Chains, Phys. Rev. Lett. **117**, 046101 (2016).

[28] A series of control experiments was performed to exclude that (i) the oxygen pressure applied in the second step or (ii) the amount of Mn deposited onto the Ir substrate plays a critical role for the formation of the $c(6 \times 2)$ and the (9×2) magnetic unit cell. These studies led to the conclusion that only the oxygen pressure during the last oxygen annealing step (step four forming MnO_x chains) determines the resulting MnO_x structure, while the other parameters do not matter in a general sense.

[29] P. Ferstl, F. Mittendorfer, J. Redinger, M. A. Schneider, and L. Hammer, Monatomic Co, CoO_2, and CoO_3 nanowires on Ir(100) and Pt(100) surfaces: Formation, structure, and energetics, Phys. Rev. B **96**, 085407 (2017).

[30] K. Reuter and M. Scheffler, Composition, structure, and stability of RuO_2(110) as a function of oxygen pressure, Phys. Rev. B **65**, 035406 (2001).

[31] J. Rogal and K. Reuter, *Ab initio* atomistic thermodynamics for surfaces: A primer, in *VT-142 RTO AVT/VKI Lecture Series*, NATO Research and Technology Organisation (Plenum, New York, 2007), pp. 2–1.

[32] M. Bode, M. Heide, K. von Bergmann, P. Ferriani, S. Heinze, G. Bihlmayer, A. Kubetzka, O. Pietzsch, S. Blügel, and R. Wiesendanger, Chiral magnetic order at surfaces driven by inversion asymmetry, Nature (London) **447**, 190 (2007).

[33] B. Schweflinghaus, B. Zimmermann, M. Heide, G. Bihlmayer, and S. Blügel, Role of Dzyaloshinskii-Moriya interaction for magnetism in transition-metal chains at Pt step edges, Phys. Rev. B **94**, 024403 (2016).

[34] T. N. Rhodin and G. Broden, Preparation and chemisorptive properties of the clean normal and reconstructed surfaces of Ir(100)–Role of multiplets, Surf. Sci. **60**, 466 (1976).

[35] T. Ali, B. Klötzer, A. V. Walker, Q. Ge, and D. A. King, Surface kinetics of a nonlinear oxygen-induced $(1 \times 5) \rightarrow (1 \times 1)$ phase transition on Ir(100), J. Chem. Phys. **109**, 9967 (1998).

[36] A. Schmidt, W. Meier, L. Hammer, and K. Heinz, Deep-going reconstruction of Ir(100)-5 $\times$ 1, J. Phys.: Condens. Matter **14**, 12353 (2002).

[37] P. Ferstl, T. Schmitt, M. A. Schneider, L. Hammer, A. Michl, and S. Müller, Structure and ordering of oxygen on unreconstructed Ir(100), Phys. Rev. B **93**, 235406 (2016).

[38] K. Johnson, Q. Ge, S. Titmuss, and D. A. King, Unusual bridged site for adsorbed oxygen adatoms: Theory and experiment for Ir100-(1 $\times$ 2)-O, J. Chem. Phys. **112**, 10460 (2000).

[39] G. Kresse and J. Hafner, *Ab initio* molecular dynamics for liquid metals, Phys. Rev. B **47**, 558 (1993).

[40] G. Kresse and J. Furthmüller, Efficiency of ab-initio total energy calculations for metals and semiconductors using a plane-wave basis set, Comput. Mater. Sci. **6**, 15 (1996).

[41] G. Kresse and D. Joubert, From ultrasoft pseudopotentials to the projector augmented-wave method, Phys. Rev. B **59**, 1758 (1999).

[42] J. P. Perdew, K. Burke, and M. Ernzerhof, Generalized Gradient Approximation Made Simple, Phys. Rev. Lett. **77**, 3865 (1996).

[43] S. L. Dudarev, G. A. Botton, S. Y. Savrasov, C. J. Humphreys, and A. P. Sutton, Electron-energy-loss spectra and the structural stability of nickel oxide: An LSDA+U study, Phys. Rev. B **57**, 1505 (1998).

[44] Information and download from https://github.com/viperleed.

[45] J. B. Pendry, Reliability factors for LEED calculations, J. Phys. C: Solid State Phys. **13**, 937 (1980).

[46] V. Blum and K. Heinz, Fast LEED intensity calculations for surface crystallography using Tensor LEED, Comput. Phys. Commun. **134**, 392 (2001).

[47] J. Rundgren, Optimized surface-slab excited-state muffin-tin potential and surface core level shifts, Phys. Rev. B **68**, 125405 (2003).

[48] P. J. Rous, J. B. Pendry, D. K. Saldin, K. Heinz, K. Müller, and N. Bickel, Tensor LEED: A Technique for High-Speed Surface-Structure Determination, Phys. Rev. Lett. **57**, 2951 (1986).

[49] J. W. Arblaster, Crystallographic properties of iridium, Platin. Met. Rev. **54**, 93 (2010).